Acta Materialia 207 (2021) 116700

Contents lists available at ScienceDirect

Acta Materialia

journal homepage: www.elsevier.com/locate/actamat

# Outstanding cracking resistance of fibrous dual phase steels

Karim Ismail[a], Astrid Perlade[b], Pascal J. Jacques[a], Thomas Pardoen[a,*]

[a] Institute of Mechanics, Materials and Civil Engineering, UCLouvain, 2 Place Sainte Barbe, 1348 Louvain-la-Neuve, Belgium
[b] ArcelorMittal Maizières Research SA, Voie Romaine, 57280 Maizières-lès-Metz, France

ARTICLE INFO

*Article history:*
Received 9 October 2020
Revised 13 December 2020
Accepted 25 January 2021
Available online 29 January 2021

*Keywords:*
Dual-phase
Fracture mechanisms
Phase morphology
Microstructures
Fracture toughness

ABSTRACT

Dual phase (DP) steels are widely used for their excellent combination of strength-ductility-cost performance. However, several forming and/or structural applications are affected by cracking resistance issues. We show here that DP steels with a 'Thomas-fibers' type platelet martensite morphology exhibit significantly larger cracking resistance compared to corresponding equiaxed microstructures. The superior cracking resistance is demonstrated both for thin and thick specimens processed with different martensite volume fractions and thicknesses. The cracking of thin sheets involves complex intermingling of work spent for crack tip necking and for material fracture as quantified using the essential work of fracture method, complemented with fractography and microstructure characterization. The better cracking resistance is shown to originate from a remarkable resistance to damage nucleation related to the alignment of the platelets upon deformation and from their small size. This finding offers a new path to optimize the fracture toughness of DP steels without compromising the strength and/or changing the chemical composition.



## 1. Introduction

Dual phase (DP) steels have long been used in the automotive industry for their excellent mechanical properties in terms of strength-ductility balance associated to low processing cost. The good compromise between strength and ductility results from the appropriate combination of ductile ferrite ($\alpha$) and hard martensite ($\alpha$'). However, many DP steels suffer from limited fracture toughness leading, for instance, to edge cracking during forming operations of precut sheets. This has been demonstrated by insufficient hole expansion capacity, which is directly related to cracking resistance [1,2]. Higher cracking resistance is thus needed to improve formability and to further improve the structural behavior of some critical DP components. There is thus a major interest for developing DP steel grades with enhanced cracking resistance but preserving the high strength-ductility balance.

The cracking resistance of materials with pre-existing defects can be characterized by the fracture toughness defined as the value of the stress intensity factor, $K_{Ic}$, or of the $J$-integral at cracking initiation, $J_{Ic}$. The fracture toughness of DP steels has not been widely investigated, only a handful of studies have provided quantitative data. For instance, the impact resistance has been determined through Charpy tests [3–7], which provides information about the dynamic cracking resistance, but the relationship with fracture toughness is not direct. Regarding quasi-static fracture toughness, three point bending tests on chevron-notched DP steels specimens were performed in [4] leading to a maximum $K_{Ic}$ of 138 MPa$\sqrt{m}$ while tensile tests on circumferentially notched specimens gave a maximum $K_{Ic}$ of 56.4 MPa$\sqrt{m}$ [8,9]. This corresponds to a $J_{Ic}$ of ~90 $kJ.m^{-2}$ and ~15 $kJ.m^{-2}$, respectively (using the relationship $J_{Ic} = K_{Ic}^2/E^*$ where $E^* = E/(1-\nu^2)$ in plane strain, with, $E$, the Young's modulus and, $\nu$, the Poisson ratio). More recently, Faccoli et al. [10] found $J_{Ic}$ ~100 $kJ.m^{-2}$ for a DP1000 steel, while Frómeta et al. [11] reported $J_{Ic}$ equal to 84 $kJ.m^{-2}$, using both CT Compact Tension (CT) and Double-Edge-Notched Tension (DENT) specimens. The fracture toughness heavily depends on the microstructure, such as on the $\alpha$' volume fracture and carbon content. A full picture of the relationship between composition, microstructure and fracture toughness in DP steels is still missing.

Recently, fibrous DP steels, also called 'Thomas fibers' DP steels [12], have been re-investigated, confirming an excellent strength-ductility ratio [13], but also promising cracking resistance compared to classical DP steels [14,15]. The objective of this work is to study the cracking resistance of 'Thomas fibers' DP steels in the form of thin sheets in comparison to reference equiaxed DP steels, as well as of some thick sheets results taken from [14]. The number of applications of DP sheets is large and justifies the focus on thin sheets.

* Corresponding author.
*E-mail address:* thomas.pardoen@uclouvain.be (T. Pardoen).

https://doi.org/10.1016/j.actamat.2021.116700
1359-6454/

The plane strain fracture toughness $J_{Ic}$ can be expressed for a ductile fracture mechanism by nucleation, growth and coalescence of voids as [16]

$$J_{Ic} = \sigma_0 X_0 F\left(\frac{\sigma_0}{E}, n, f_0, W_0, \lambda_0\right), \quad (1)$$

where $\sigma_0$ is the yield stress, $X_0$ is an internal length scale related to the void spacing, and $F$ is a function depending on the ratio $\frac{\sigma_0}{E}$, strain-hardening exponent $n$, initial void porosity $f_0$, initial void aspect ratio $W_0$, and void spacing distribution $\lambda_0$. A combination of a high strength $\sigma_0$ and a high fracture strain $\varepsilon_f$ (which will result from low initial porosity and late void nucleation for instance) does not necessarily lead to a high $J_{Ic}$; the internal length scale, $X_0$, related to the microstructure plays a major role as well, as demonstrated in [16].

In near plane stress conditions, typical of thin ductile metallic sheets, Eq. (1) must be modified to introduce the effect of thickness [17]. This is due to the additional contribution from crack tip necking to the cracking resistance, which depends on thickness. As an alternative to $J_{Ic}$, the essential work of fracture (EWF), $w_e$, is often used to characterize thin sheet cracking. The EWF method has already been applied on various DP steels with equiaxed microstructures, for instance by [1,18-23], but never reported on 'Thomas fibers' DP steels. The EWF characterizes the cracking resistance as the average energy per unit area spent in the fracture process zone (FPZ) all along the cracking process. In thin metallic sheets, the stress state is close to plane stress which favors the development of crack tip necking. The necking work varies with thickness and the EWF is thus not a truly intrinsic property in this regime (nor $J_{Ic}$) [17]. The EWF can be further separated in terms of an intrinsic work spent for damage and fracture, noted $\Gamma_0$, and an average work spent in necking, noted $\Gamma_n$ [17,24,25]:

$$w_e = \Gamma_0 + \Gamma_n = \Gamma_0 + \beta t_0 w_n, \quad (2)$$

where $w_n$ is an average work of necking per unit volume and $\beta$ a shape factor associated to the necking zone. In other words, thin sheets of different materials must be tested at the same thickness to provide a fair basis of comparison in terms of cracking resistance as quantified with the EWF. But, a full picture regarding the resistance to cracking of ductile thin sheets can only be obtained by looking at the separation between $\Gamma_0$ and $\Gamma_n$, and thus at a range of thicknesses.

The analysis of the EWF and of the two terms $\Gamma_0$ (which can be assimilated to $J_{Ic}$ in Eq. (1)) and $\Gamma_n$ sets the fundamental basis for relating the cracking resistance to the strength ($\sigma_0$), ductility ($\varepsilon_f$), microstructure ($X_0$, $f_0$ and $W_0$) and thickness, which we aim at elucidating here in the context of 'Thomas fibers' versus equiaxed DP steels. For this purpose, both equiaxed and 'Thomas fibers' microstructures were processed with various $\alpha$' contents and thicknesses. The damage and cracking resistance were systematically characterized in addition to the elastoplastic properties. In particular, the EWF method has been used to compare the equiaxed and fibrous versions of DP steels. Earlier data obtained on thick specimens were added for the sake of comparison. Hole expansion tests were performed to verify the positive impact of the 'Thomas fibers' morphology on a forming application.

## 2. Materials and experimental procedure

### 2.1. As-received materials and processing

The equiaxed DP steels were generated by intercritical annealing, followed by water quenching (to induce the transformation of austenite into $\alpha$') of cold-rolled sheets. On the other hand, the 'Thomas fibers' versions [12] were processed by intercritical annealing of a fully $\alpha$' microstructure. The reversion of $\alpha$' induces the nucleation and growth of austenite at the prior lath interfaces. Fig. 1 shows examples of the two microstructures with the corresponding heat treatments.

**Table 1**
Chemical composition (in wt %) of the as-received steel grade used for thin sheet samples.

| C | Mn | Si | Cr | Al | P | S |
|---|---|---|---|---|---|---|
| 0.045 | 2 | 0.3 | 0.4 | 0.028 | 0.013 | 0.0025 |

**Table 2**
Temperature and duration of the applied thermal treatments for thin sheets, each step being ended by water quenching.

| | *Austenitization* | *Intercritical annealing* |
|---|---|---|
| **eV19t1 & eV19t2** | / | 735°C – 7 min |
| **eV36t1 & eV36t2** | / | 785°C – 7 min |
| **pV19t1 & pV19t2** | 1100°C – 17 min | 760°C – 7 min |
| **pV36t1 & pV36t2** | 1100°C – 17 min | 785°C – 7 min |

**Table 3**
Chemical composition (in wt %) of the as-received steel grades used for the bulk samples.

| | C | Mn | Si | Cr | Al | P | S |
|---|---|---|---|---|---|---|---|
| 1) | 0.023 | 2.05 | 0.31 | 0.405 | 0.038 | 0.012 | 0.003 |
| 2) | 0.045 | 2 | 0.3 | 0.4 | 0.028 | 0.013 | 0.0025 |
| 3) | 0.088 | 2.07 | 0.305 | 0.435 | 0.036 | 0.0025 | 0.0025 |

**Table 4**
Temperatures and durations of the applied heat treatments for thick sheets, each step being ended by water quenching.

| | *Austenitization* | *Intercritical annealing* |
|---|---|---|
| **pV17t10** | 1100°C – 15 min | 720°C – 20 min |
| **pV21t10** | 1100°C – 15 min | 735°C-20 min |
| **pV14t10** | 1100°C – 15 min | 702°C-1380 min |
| **pV32t10** | 1100°C – 15 min | 760°C-20 min |

**Thin DP steel sheets.** The different microstructures were processed from the same initial 12 mm thick ferrite-pearlite wrought plate of homogenized chemical composition given in Table 1. Pieces of this plate were first hot-rolled down to a thickness of 5 mm after reheating at 1100°C, followed by cold-rolling down to the investigated thicknesses (i.e. 0.5, 1 and 2 mm, respectively). The heat treatments summarized in Table 2 were performed after cold-rolling in order to generate the equiaxed and 'Thomas fibers' microstructures. The austenitization was performed in a muffle furnace followed by water quenching. The intercritical annealing was made in a fluidized bed furnace ensuring a mean heating rate of 50 $^{\circ}C.s^{-1}$, followed by water quenching. The different samples are labeled in the following as $x$Vytz, with $x$ being either e or p for equiaxed or 'Thomas fibers' (with "p" for platelet), $y$ being the $\alpha$' volume fraction (in %), and $z$ being the sheet thickness (in mm), respectively.

**Thick DP steel specimens.** In addition, three grades were investigated in an earlier study [13,14] to generate four DP steels in the form of 10 mm thick samples, see Table 3. Different heat treatment conditions summarized in Table 4 were applied in order to generate microstructures similar to the thin sheets. The labelling is similar: pV17t10 with composition 1, pV21t10 and pV32t10 with composition 2, and pV14C63 with composition 3 of Table 3. More details can be found in [13,14].

### 2.2. Microstructures

Fig. 2 is a panel of SEM micrographs of the microstructures after polishing and Nital etching. A 3D microstructure characteriza-

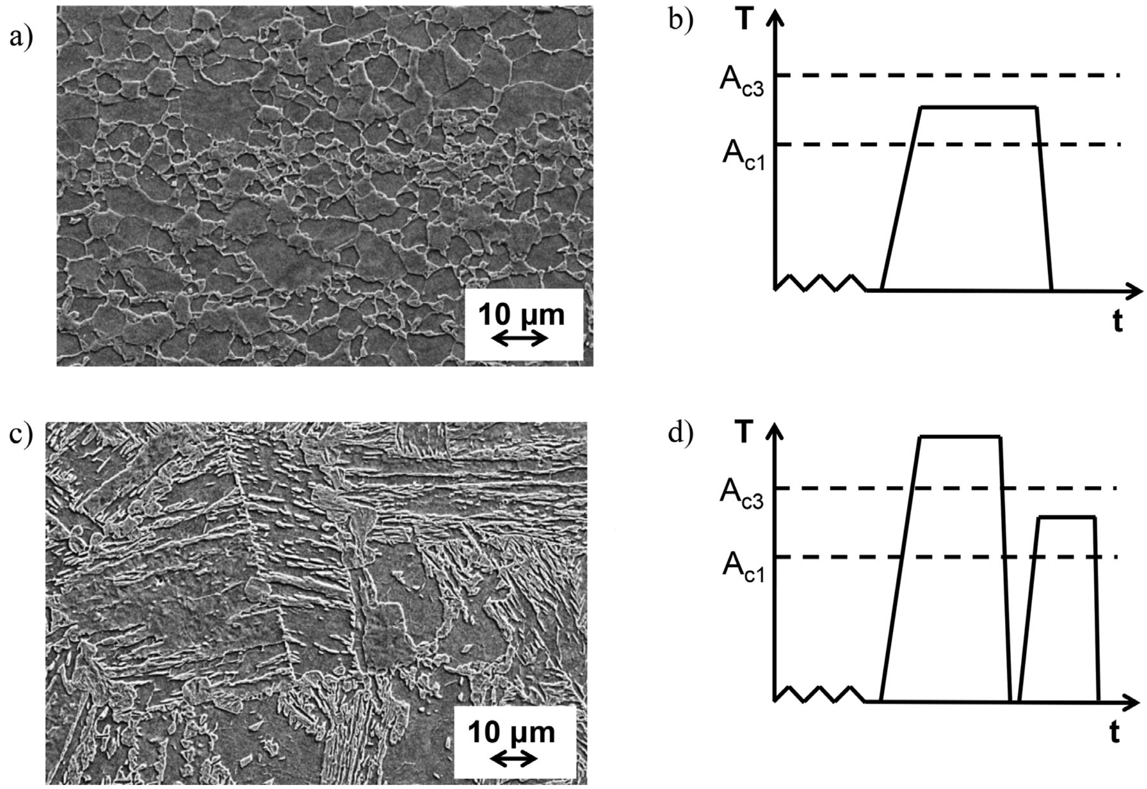


**Fig. 1.** Equiaxed (a) and 'Thomas fibers' (c) microstructures with the corresponding heat treatments (b) and (d).

tion was additionally carried out on a 10 mm thick plate. A serial sectioning procedure was performed using Vickers indents both for the positioning and for the estimation of the amount of removed material. A superposition of 2D images led to the 3D reconstruction of the 'Thomas fibers' microstructure shown in Fig. 3, revealing that the $\alpha$' particles of the 'Thomas fibers' microstructure exhibit, as expected, a platelet shape.

### 2.3. Uniaxial tensile tests

Uniaxial tensile tests were conducted using a Zwick-Roell 50kN universal tensile testing machine under displacement control at constant crosshead speed of 1 mm.min$^{-1}$ and under controlled temperature and humidity of 23°C and 49%, respectively. The loading direction was aligned with the rolling direction. An extensometer was used with an initial gauge length at least equal to 20 mm. The 0.2% yield stress, $\sigma_{0.2\%}$, true ultimate tensile strength, $\sigma_u$, and true strain at necking, $\varepsilon_u$, were extracted, with the onset of necking taken at maximum load. The values were determined from each test independently, with the mean and standard deviation calculated afterwards. The true fracture strain, $\varepsilon_f$, was measured post-mortem on the broken specimens and determined from

$$\varepsilon_f = \ln\left(\frac{A_0}{A_f}\right), \tag{3}$$

where $A_0$ and $A_f$ are the initial and final projected area of the fracture surface, respectively. The fracture stress, $\sigma_f$, was calculated as the ratio between the load at fracture, $F_f$, and final area, $A_f$.

### 2.4. Essential work of fracture

The standards for the measurement of $K_{Ic}$, $G_{Ic}$ and $J_{Ic}$ impose a minimum thickness that can usually not be met when investigating the cracking resistance of tough metallic sheets due to extensive plasticity. As explained in the introduction, the EWF method, proposed by Cotterell and Reddel [26], is an appropriate alternative. The Double-Edge-Notched Tension (DENT) geometry shown in Fig. 4 was used. Upon loading, two zones must be distinguished: (i) the FPZ in which necking, damage and fracture occurs, and (ii) the diffuse plastic zone (DPZ). The total work of fracture, $W_f$, is written as the sum of the plastic work spent in the DPZ, $W_p$, and of the work spent in the FPZ, $W_e$:

$$W_f = W_e + W_p. \tag{4}$$

The EWF method is based on dimensional considerations: (i) the area of the DPZ, hence $W_p$, is proportional to $l_0^2$, with $l_0$ being the initial ligament length (see Fig. 4); while (ii) the FPZ size, and thus $W_e$, is proportional to $l_0$. Hence, the total work of fracture, $W_f$, can be expressed as

$$W_f = l_0 t_0 w_e + \alpha l_0^2 t_0 w_p, \tag{5}$$

where $w_e$ is the work spent per unit area within the FPZ, defined as the EWF; $w_p$ is the average plastic work spent in the DPZ per unit volume, $t_0$ is the initial thickness, and $\alpha$ is a shape factor. The specific work of fracture, $w_f$, is obtained by dividing $W_f$ by the initial ligament area:

$$w_f = \frac{W_f}{l_0 t_0} = w_e + \alpha l_0 w_p. \tag{6}$$

In practice, DENT specimens with various $l_0$ are deformed until final fracture. The integration of the load-displacement response provides $W_f$ for the different $l_0$. Based on Eq. (6) and illustrated in Fig. 4, a linear regression on the $w_f$ versus $l_0$ data allows the separation of $w_e$ and $\alpha w_p$. Then, Eq. (2) can further be used to separate the necking and fracture contributions to $w_e$.

The conditions of validity of the EWF method have been determined, e.g. [26,28–31], and translated mainly into restrictions on $l_0$; that is, $l_0$ must be in an interval between a lower bound of admissible ligament length, $l_{min}$, and upper bound, $l_{max}$, that are

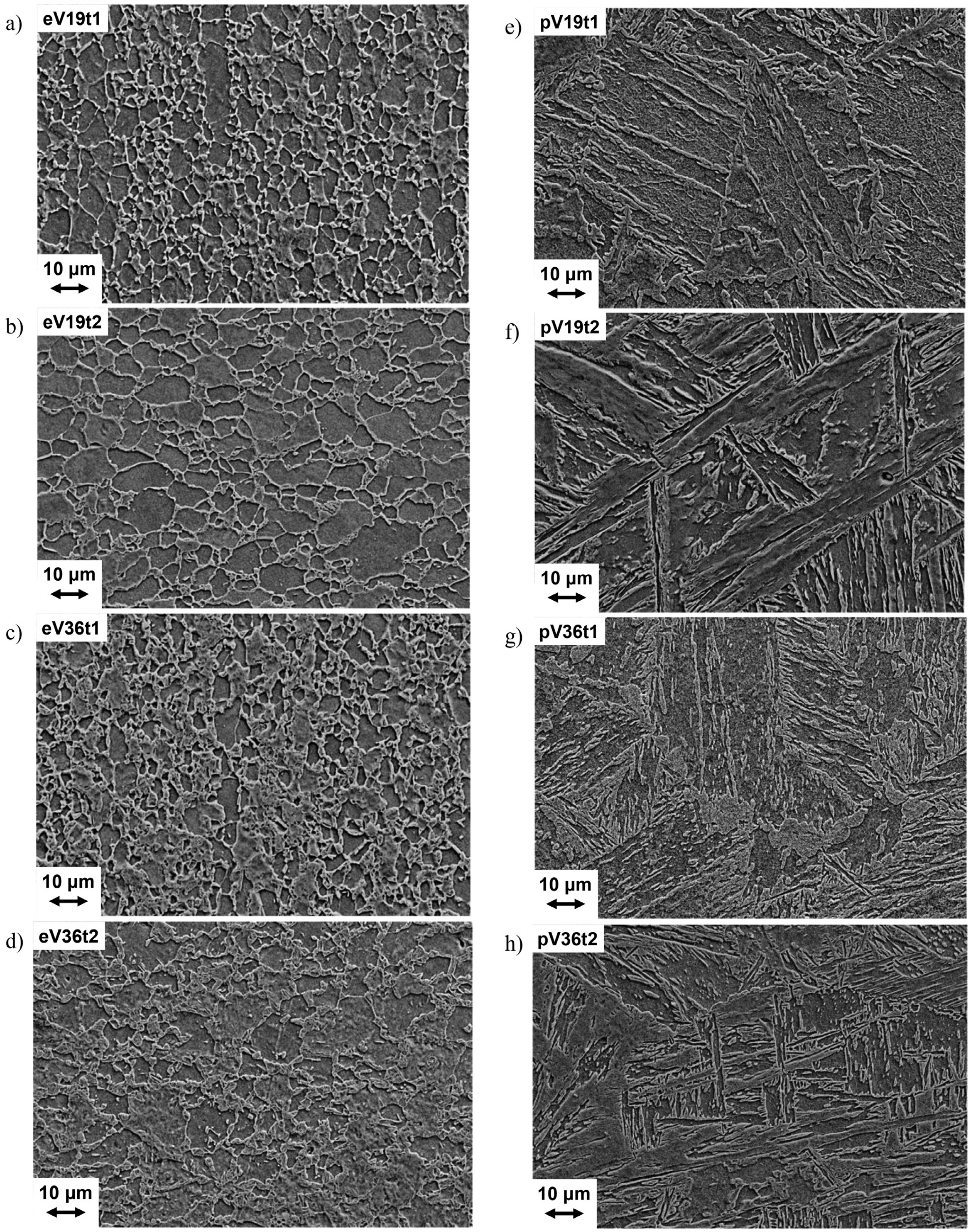


**Fig. 2.** SEM micrographs of all investigated microstructures: a) eV19t1, b) eV19t2, c) eV36t1, d) eV36t2, e) pV19t1, f) pV19t2, g) pV36t1, h) pV36t2, i) pV17t10, j) pV21t10, k) pV14t10, l) pV32t10.

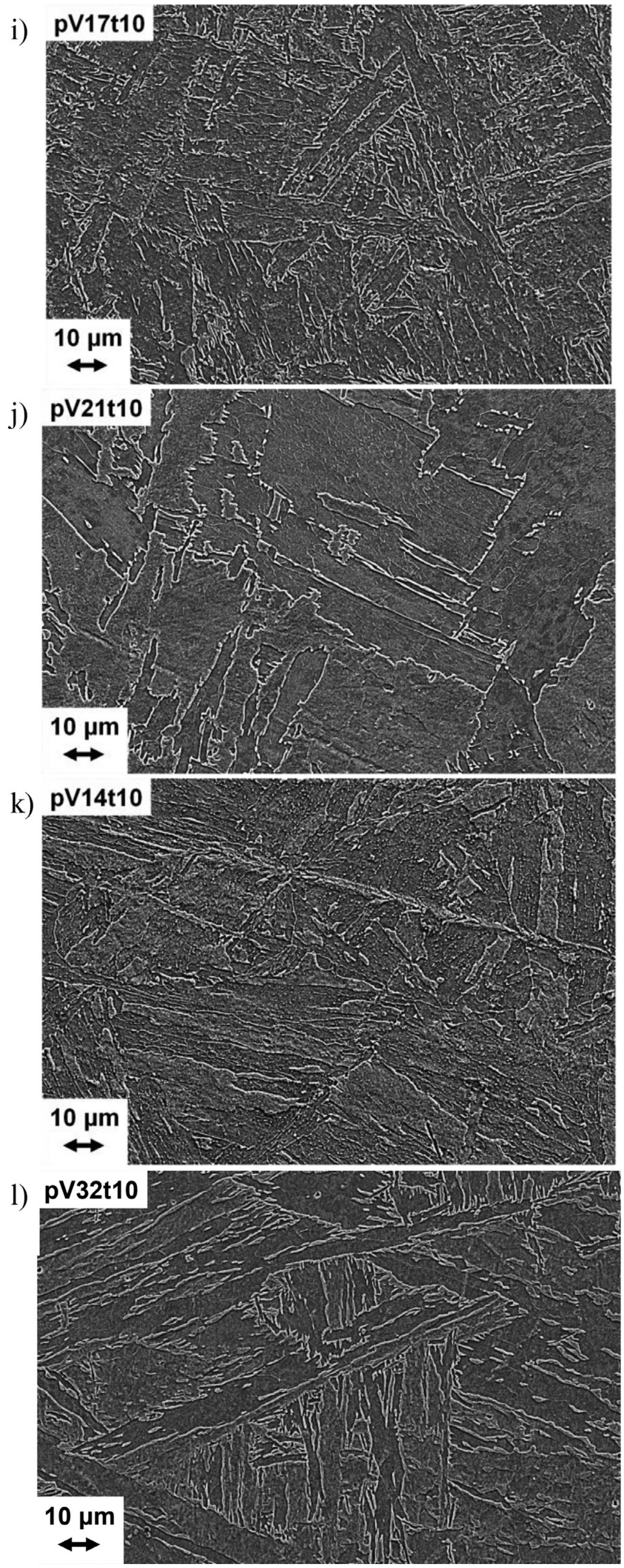


**Fig. 2.** Continued

expressed as

$$l_{\min} = (3...5)t_0 \leq l_0 \leq \min(L/3; r_p) = l_{\max}, \quad (7)$$

where $L$ corresponds to the width and where $r_p$ is the plane stress plastic zone size equal to

$$r_p = \frac{1}{\pi}\left(\frac{K}{\sigma_0}\right)^2 \approx \frac{1}{\pi}\frac{Ew_e}{\sigma_0^2}, \quad (8)$$

where $K$ is the stress intensity factor.

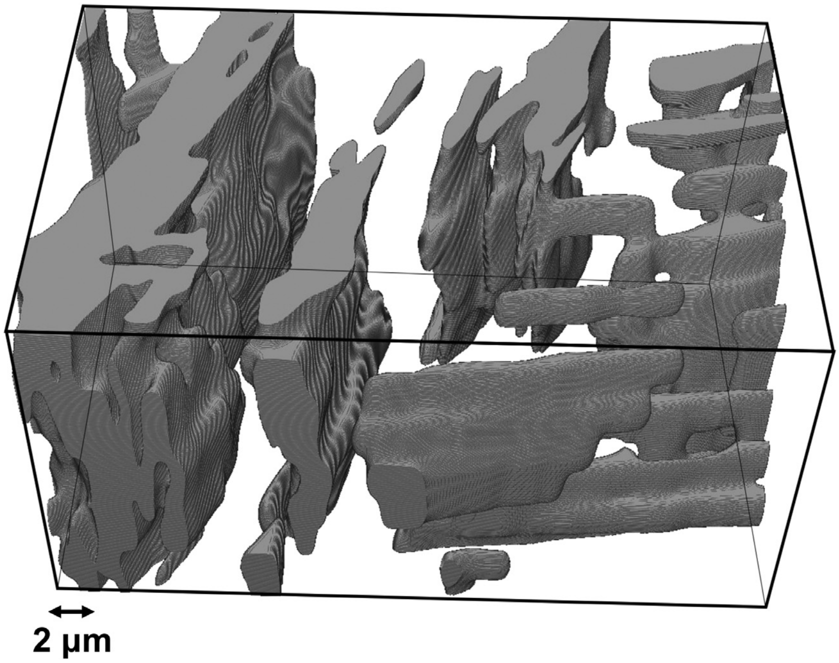


**Fig. 3.** 3D reconstruction of the morphology of the martensite present in the 'Thomas fibers' microstructure based on a superposition of 2D SEM micrographs.

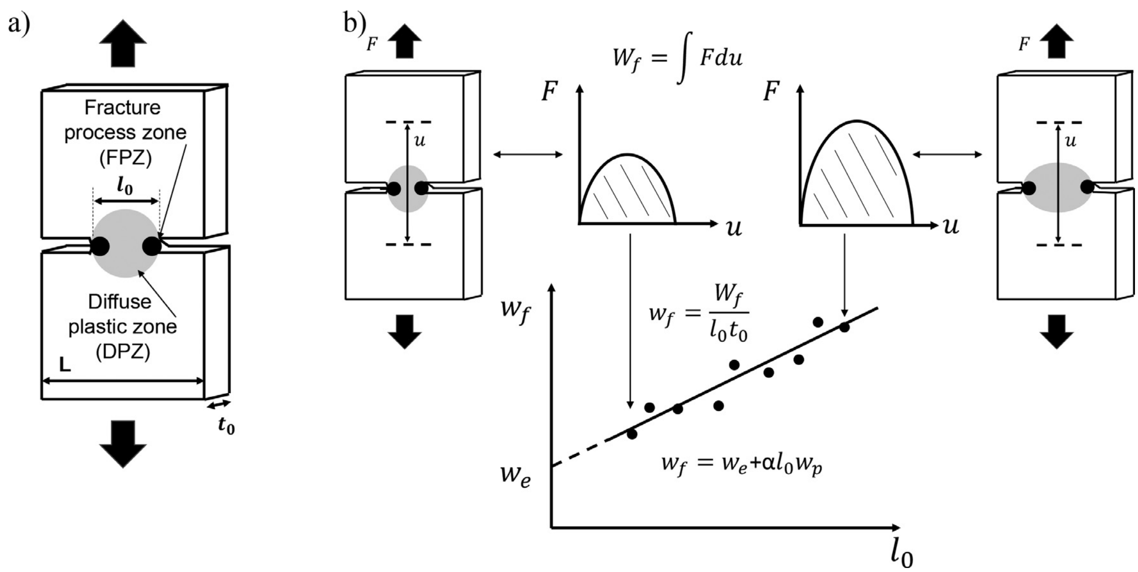


**Fig. 4.** Schematic representation of DENT sample with the illustration of the diffuse plastic zone (DPZ) and the fracture process zone (FPZ) (a) and illustration of the EWF method (b) (inspired from [27]).

The EWF method was applied to all microstructures and thicknesses using DENT specimens 100 mm long, and 50 mm wide, tested parallel to rolling direction. In order to fulfill the validity requirements, $l_0$ was varied between 5 and 15 mm for the 0.5 mm thick sheets, from 5 to 17.5 mm for the 1 mm thick sheets, and from 9 to 15 mm for the 2 mm thick sheets. Notches with an initial opening of around 250 to 300 $\mu$m were reached by electrical discharge machining. In order to avoid time-consuming fatigue precracking (while ensuring an initial crack tip smaller than the critical opening, as verified after testing), crack tip sharpening was induced with a razor blade, leading to a crack tip radius between 50 and 100 $\mu$m. The razor blade cutting can affect the microstructure through local work hardening and damage, which, in turn, can affect the crack initiation energy. However, as the work dissipated during initiation only mildly contributes to the total work when $l_0$ is sufficiently long, this procedure does not significantly impact the EWF.

The specimens were deformed in tension until completion of cracking at a crosshead speed of 1 mm.min$^{-1}$. Displacement was measured by means of an extensometer with an initial gauge length between 25 and 50 mm. The standard deviation on $w_e$ was calculated from the least square method. The error analysis is described in Supplementary Materials.

### 2.5. Determination of the CTOD

The Crack Tip Opening Displacement (CTOD) at initiation, $\delta_c$, which is the critical opening at which the cracking starts, was determined by Pierman [14] using the methodology proposed in [32]. It consists in measuring the difference between the total crack

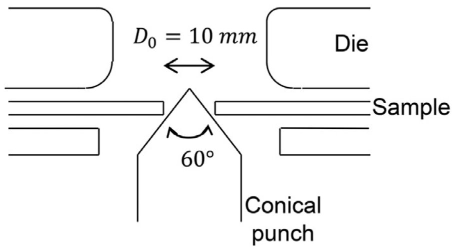


**Fig. 5.** Hole expansion test configuration.

opening after blunting and the extra opening due to crack propagation. Following the measurement for different crack extensions, an extrapolation to zero crack extension leads to $\delta_c$, which is related to $J_{Ic}$ through

$$\delta_c = d\frac{J_{Ic}}{\sigma_0}, \tag{9}$$

where $d$ is the Shih factor [33]. This method was applied to the thick specimens only to estimate $J_{Ic}$.

### 2.6. Hole expansion tests

Hole expansion tests, schematized in Fig. 5, were performed to determine the stretch flangeability of eV19t1, eV36t1, pV19t1 and pV36t1 samples. The specimens were first punched to produce holes of 10 mm in diameter. The specimens were then clamped burr up with a load of 150 kN in a blank holder and the holes were expanded by a 60° conical punch moving at a speed of 0.8 mm/s. The tests were stopped as soon as a crack was detected through the thickness of the sample. The inner diameter of the expanded holes was measured in two perpendicular directions, while avoiding cracks. The hole expansion ratio, λ, expressed in percent, is defined as

$$\lambda = 100\frac{\overline{D_h} - D_0}{D_0}, \tag{10}$$

where $\overline{D_h}$ is the average diameter of the expanded hole and $D_0$ is the initial hole diameter. The hole expansion ratios are the result of an averaging on seven specimens.

### 2.7. Damage characterization

The broken uniaxial tension and DENT specimens were prepared for damage characterization involving SEM analysis of the fracture surfaces. The thickness reduction factor, $r_f$, and the average equivalent fracture strain, $\varepsilon_{f,eq}$, of the DENT specimens are expressed as

$$r_f = \frac{t_0 - t_f}{t_0}, \tag{11}$$

$$\varepsilon_{f,eq} = \frac{2}{\sqrt{3}}\ln\left(\frac{t_0}{t_f}\right), \tag{12}$$

where $t_f$ is the final thickness at mid-ligament. Both the DENT and broken uniaxial tension samples were cut at mid-width and mounted to allow transverse observations on sections below the fracture surface, as shown on Fig. 6. The surface was polished down to 1 $\mu$m, followed by an OPA polishing step of 20 min and by an ultrasonic bath cleaning of 10 min to remove potential residues. OPA was occasionally sufficient to reveal the microstructure by SEM. In the case of a too thick passivation layer, samples were etched using a Nital solution.

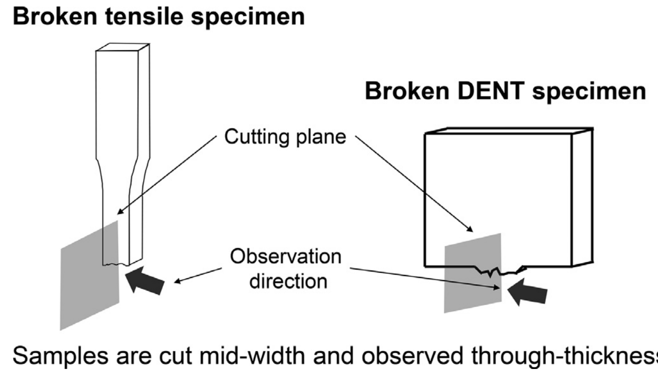


**Fig. 6.** Schematic representation of the damage characterization procedure in broken uniaxial tensile and DENT specimens.

## 3. Results

### 3.1. Uniaxial tensile tests

Figs. 7(a) and (b) show the average true stress – true strain curves over 2 to 5 replicas of equiaxed and platelet microstructures for 1 mm thick (full lines) and 2 mm thick (dotted lines) specimens. All curves are given in Supplementary Materials. Fig. 7(b) is a zoom on the response up to necking while Fig. 7(a) adds the points corresponding to the true fracture strain and true fracture stress, $\varepsilon_f$ and $\sigma_f$, of each condition. The dotted lines joining the necking and fracture points offer a qualitative view on the strain-hardening capacity at large strains. The linear evolution is an approximation of the (unknown) real behavior, while noting that a post-necking linear variation is often observed in many metallic alloys, e.g. [34]. As a matter of fact, $\sigma_f$ is an upper bound of the true equivalent stress at fracture due to the generation of transverse stress components during necking, but the same approximation applies to all conditions making the comparisons relevant. Fig. 7(c) shows representative stress-strain curves up to the onset of necking of the thick sheet specimens. The original curves can be found in [13]. Table 5 summarizes the main mechanical properties extracted from these curves as well as $\varepsilon_f$, $\sigma_f$ and the product $\varepsilon_f\sigma_f$.

The yield and tensile stress increase with $\alpha$' volume fraction. The 1 mm thick sheets generally exhibit a strength ~10% higher compared to the 2 mm thick sheets for the same $\alpha$'volume fraction in equiaxed microstructures. This results from slight differences in microstructure, inherent of different thicknesses. The strength is higher in the platelet DP steels compared to the equiaxed ones for a $\alpha$' volume fraction of 19%, but the opposite is found for 36% $\alpha$'. On the other hand, the fracture strain is higher for the platelet morphology, except for the eV19t2 - pV19t2 cases.

### 3.2. Essential work of fracture

The load - displacement curves of the DENT specimens are given in the Supplementary Materials. When normalized by the maximum force, $F_{max}$, and maximum displacement, $u_{max}$, the curves superimpose well, which indicates the validity of the method. 2D digital image correlation was performed as an additional validity check to confirm that the plastic zone is confined between the two notches with a fully yielded ligament (see Supplementary Materials for more information).

Fig. 8 shows, for all microstructures, the variations of $w_f$ with respect to $l_0$ and the linear regressions used to extract the EWF, together with the regression coefficient $\overline{R^2}$. Some results must be interpreted with care, namely pV19t2, pV36t0.5 and eV36t1, because of either a small regression coefficient and/or a limited number of samples and/or a missing sample at the largest $l_0$.

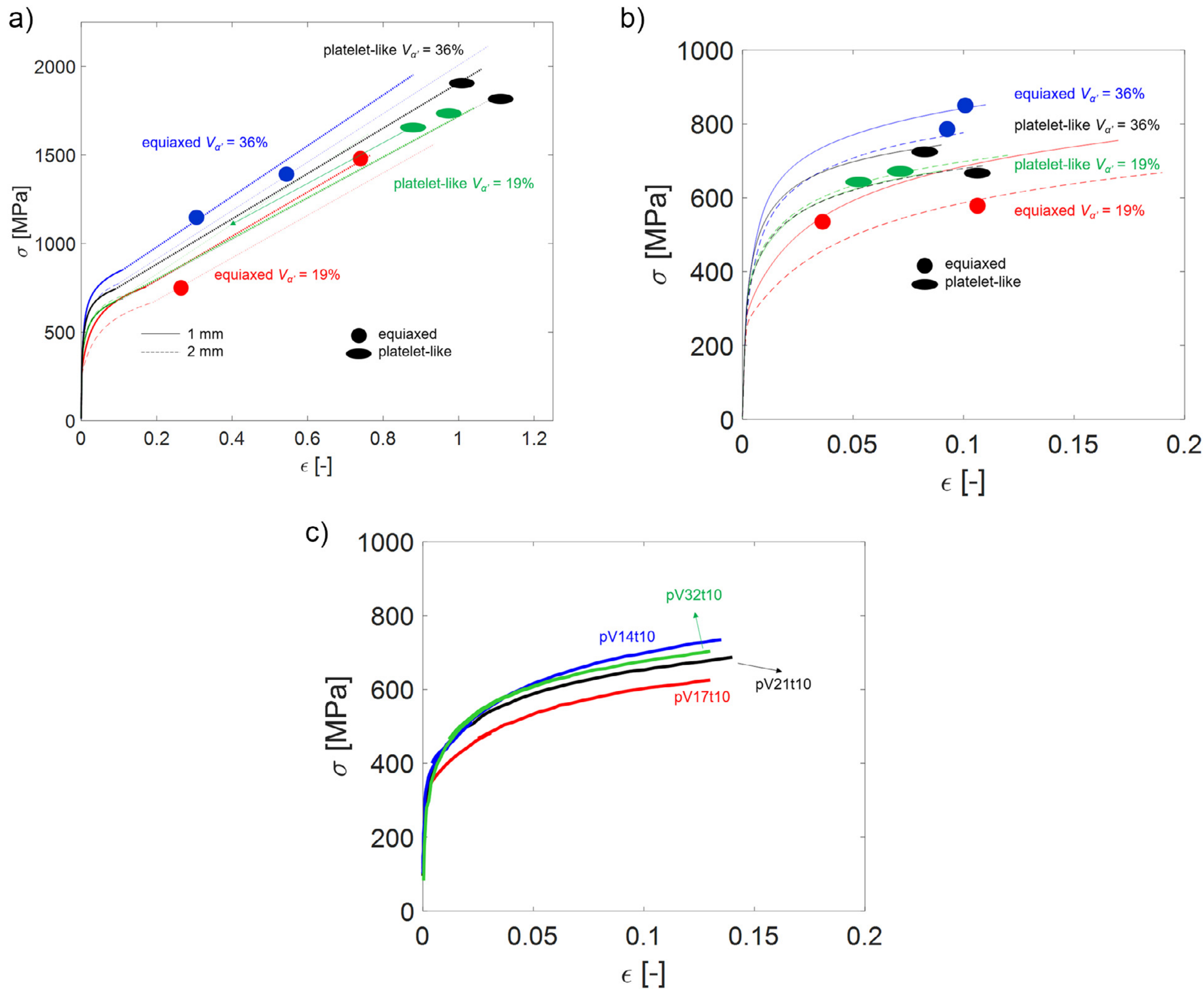


**Fig. 7.** Experimental true stress-true strain curves of the different microstructures in the case of (a) thin sheets up to the fracture point; (b) thin sheets with zoom up to necking, and (c) thick sheets (data taken from [13]). In (a), bold full lines are for 1 mm thick sheets, and dashed lines are for 2 mm thick sheets.

**Table 5**
Tensile properties of the steels.

| | $\sigma_{0.2\%}$ [MPa] | $\varepsilon_u$ [-] | $\sigma_u$ [MPa] | $\varepsilon_f$ [-] | $\sigma_f$ [MPa] | $\varepsilon_f\ \sigma_f$ [MPa] |
|---|---|---|---|---|---|---|
| **eV19t1** | 311 ± 4 | 0.17 ± 0.01 | 752 ± 6 | 0.765 ± 0.007 | 1497 ± 52 | 1075 ± 160 |
| **eV36t1** | 417 ± 9 | 0.11 ± 0.01 | 854 ± 13 | 0.88 ± 0.096 | 1953 ± 163 | 1733 ± 319 |
| **pV19t1** | 396 ± 10 | 0.09 ± 0.01 | 700 ± 27 | 1.04 ± 0.023 | 1765 ± 175 | 1852 ± 212 |
| **pV36t1** | 415 ± 7 | 0.09 ± 0.005 | 741 ± 11 | 1.06 ± 0.12 | 1984 ± 98 | 2105 ± 343 |
| **eV19t2** | 274 ± 4 | 0.19 ± 0.0002 | 666 ± 4 | 0.935 ± 0.025 | 1561 ± 37 | 1460 ± 75 |
| **eV36t2** | 367 ± 9 | 0.1 ± 0.02 | 775 ± 40 | 1.08 ± 0.156 | 2117 ± 235 | 2264 ± 422 |
| **pV19t2** | 385 ± 2.5 | 0.12 ± 0.005 | 716 ± 9 | 0.76 ± 0.04 | 1618 ± 137 | 1239 ± 173 |
| **pV36t2** | 369 ± 5 | 0.11 ± 0.02 | 688 ± 26 | 1.09 ± 0.09 | 1820 ± 110 | 1982 ± 271 |
| **pV17t10** | 342 ± 2 | 0.13 ± 0.013 | 626 ± 10 | 1.54 ± 0.1 | | |
| **pV21t10** | 345 ± 10 | 0.14 ± 0.03 | 687 ± 20 | 1.2 ± 0.15 | | |
| **pV14t10** | 494 ± 25 | 0.135 ± 0.005 | 735 ± 10 | 1 ± 0.04 | | |
| **pV32t10** | 351 ± 75 | 0.13 ± 0.01 | 704 ± 20 | 1.21 ± 0.21 | | |

Fig. 9 shows the variation of $w_e$ as a function of thickness. The EWF significantly increases with thickness for a given $\alpha$' volume fraction and morphology. The EWF of the platelet morphology is systematically larger than the corresponding equiaxed morphology by typically 50% (except for the 1 mm thick specimen with 36% $\alpha$', showing a smaller improvement). This is the core result of this study, which motivated further analysis and the discussion to come. Table 6 provides the contribution of necking $\beta w_n$ and of

**Table 6**
$\Gamma_0$ and $\beta w_n$ of equiaxed and platelet-like microstructures.

| | $\Gamma_0$ [$kJ/m^2$] | $\beta w_n$ [$kJ/m^3$] |
|---|---|---|
| eV19 | 38 ± 86 | 157 ± 69 |
| **eV36** | 137 ± 29 | 115 ± 46 |
| **pV19** | 140 ± 98 | 215 ± 111 |
| **pV36** | 56 ± 87 | 267 ± 72 |

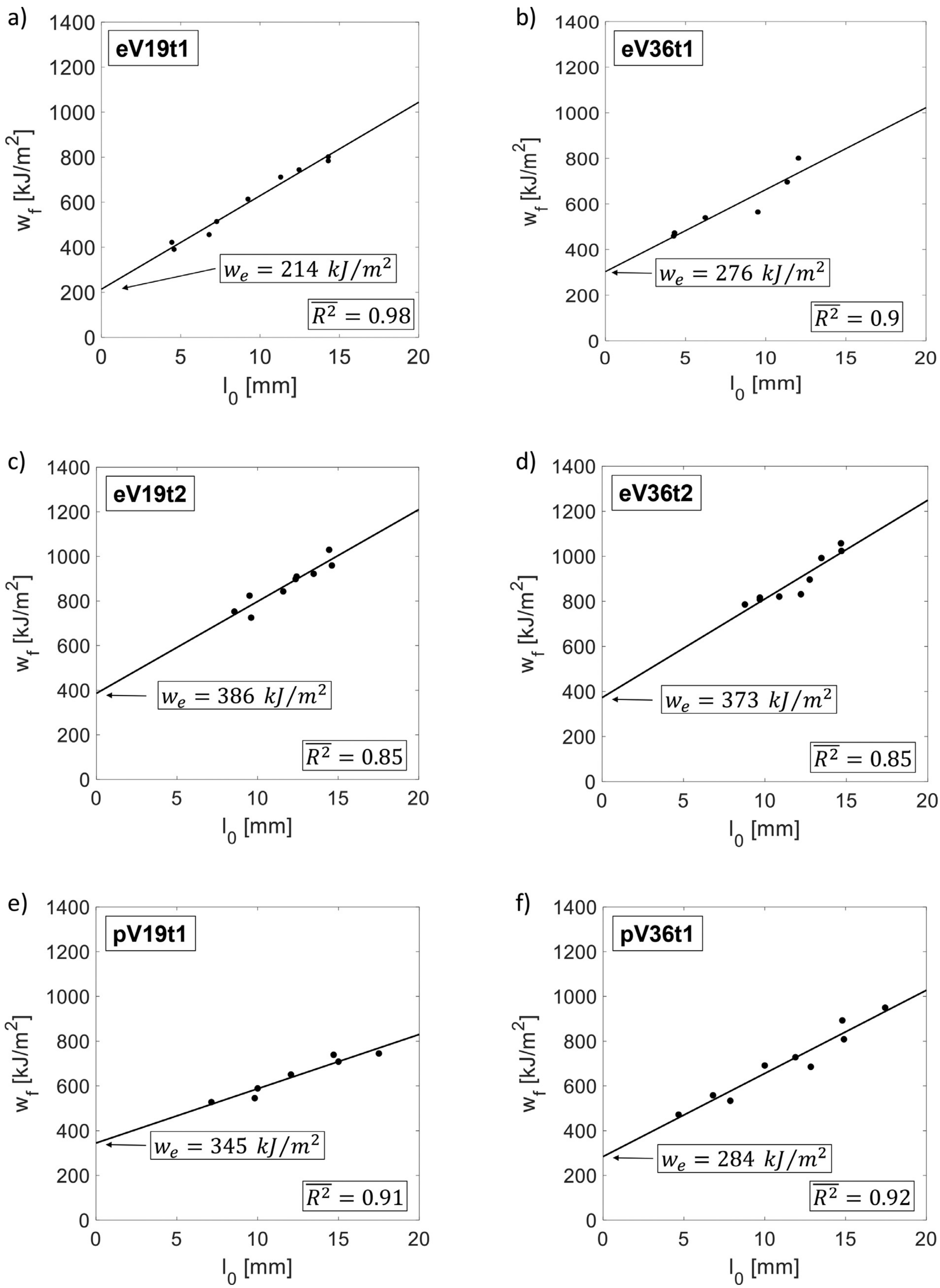


**Fig. 8.** Variation of $w_f$ as a function of $l_0$, together with the $w_e$ and the quality of the linear regressions as quantified by $\overline{R^2}$ for a) eV19t1, b) eV36t1, c) eV19t2, d) eV36t2, e) pV19t1, f) pV36t1, g) pV19t2, h) pV36t2, i) pV19t0.5, j) pV36t0.5.

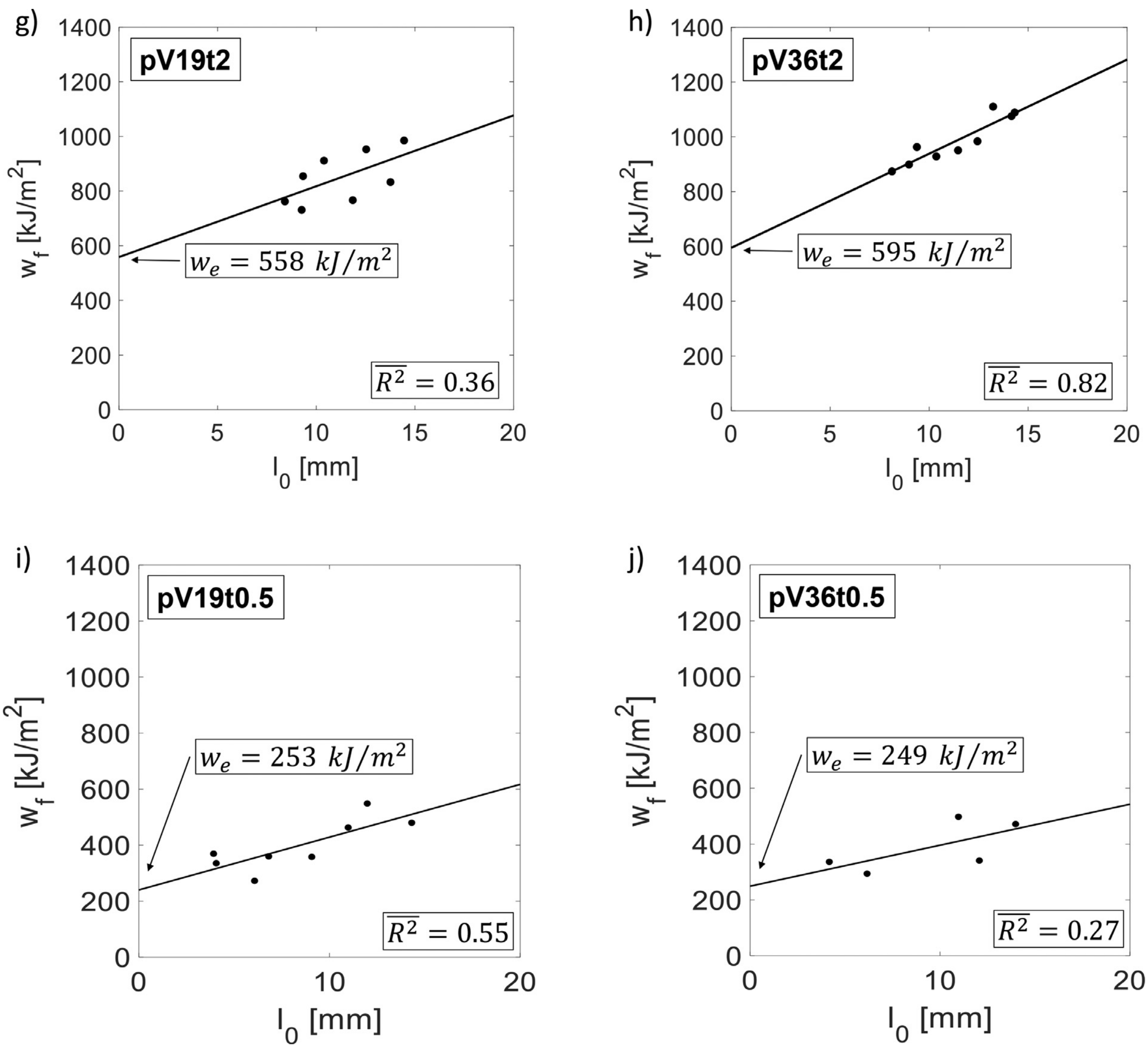


**Fig. 8.** Continued

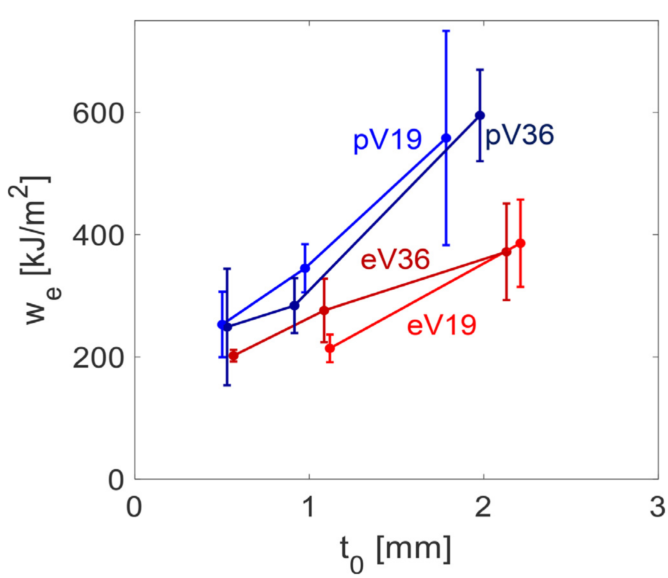


**Fig. 9.** Essential work of fracture, $w_e$, as a function of initial sheet thickness, $t_0$.

damage $\Gamma_0$ to the EWF from Eq. (2). The separation of these two energy contributions is only semi-quantitative in view of the limited number of thicknesses that were tested, leading to significant uncertainty, but the main trends are still worth being explored. The necking work $\beta w_n$ is higher for the platelet morphology, especially for the 36% $\alpha$' condition for which the difference is statistically valid. The error on $\Gamma_0$ is too large to allow any quantitative conclusions to be taken. This error propagates from the error already significant for some $w_e$ values.

### 3.3. Fracture toughness of thick sheets

The fracture toughness, $J_{Ic}$, of the four thick microstructures was determined by Pierman [14] from $\delta_c$ using Eq. (11). Table 7 gathers the $\delta_c$, corresponding Shih factors, yield strength and estimated $J_{Ic}$. In order to assess the error associated to $J_{Ic}$, the experimental error due to the measurement of $\delta_c$ is around 50 microns. These results confirm the higher cracking resistance of DP steels with platelet-like $\alpha$' morphology: the cracking resistance level, between 391 and 432 $kJ.m^{-2}$, is outstanding and much higher than what has been measured in conventional DP steels. These results were not reported yet in the literature.

**Table 7**
Fracture toughness, $J_{Ic}$, and values of the parameters used for the determination of $J_{Ic}$ for the four thick sheets microstructures.

| | $\delta_c$ [$\mu m$] | $d$ [−] | $\sigma_0$ [$MPa$] | $J_{Ic}$ [$kJ/m^2$] |
|---|---|---|---|---|
| **pV17t10** | 800 ± 50 | 0.68 | 342 ± 2 | 402 ± 21 |
| **pV21t10** | 850 ± 50 | 0.75 | 345 ± 10 | 391 ± 26 |
| **pV14t10** | 612 ± 50 | 0.7 | 494 ± 25 | 432 ± 42 |
| **pV32t10** | 592 ± 50 | 0.71 | 351 ± 75 | 351 ± 67 |

**Table 8**
Thickness reduction factor, $r_f$, and average equivalent fracture strain, $\varepsilon_{f,eq}$, of the DENT specimens for the eight thin sheet microstructures.

| | $r_f$ [-] | $\varepsilon_{f,eq}$[-] |
|---|---|---|
| **eV19t1** | 0.52 | 0.84 |
| **pV19t1** | 0.61 | 1.07 |
| **eV36t1** | 0.62 | 1.11 |
| **pV36t1** | 0.61 | 1.09 |
| **eV19t2** | 0.44 | 0.67 |
| **pV19t2** | 0.53 | 0.87 |
| **eV36t2** | 0.48 | 0.76 |
| **pV36t2** | 0.59 | 1.04 |

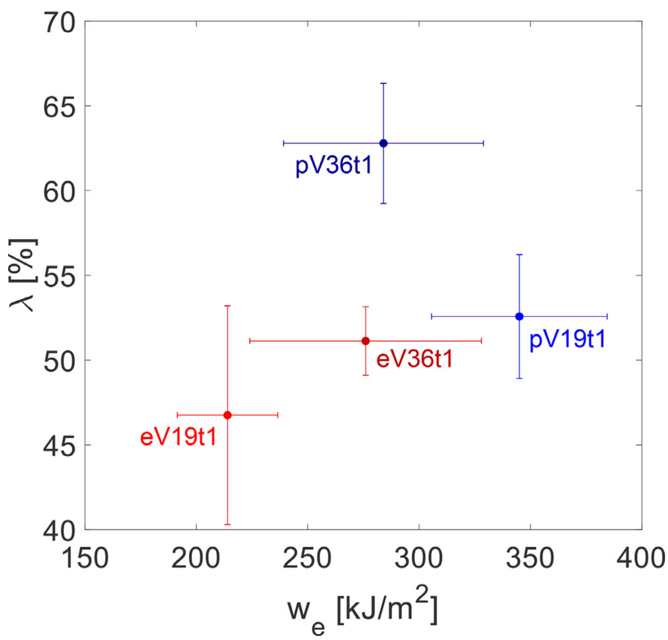


**Fig. 10.** Hole expansion ratio values, λ, as a function of the essential work of fracture for the eV19t1, eV36t1, pV19t1 and pV36t1 microstructures.

### 3.4. Hole expansion tests

Fig. 10 provides the values of the hole expansion ratio for the eV19t1, eV36t1, pV19t1, pV36t1 microstructures as a function of the EWF. The hole expansion ratio for the platelet morphology is systematically higher than for the equiaxed morphology in line with the higher EWF, anticipating the benefits for forming applications.

### 3.5. Fracture surface analysis and damage characterization

Fig. 11 shows SEM micrographs of the fracture surfaces of the tensile specimens. These SEM micrographs exhibit a classical dimple morphology, showing that all eight microstructures fail by ductile failure through a process of nucleation, growth and coalescence of primary voids. The fracture surface of samples pV19t1 and pV36t1 exhibit a slant mode, explaining the distorted shape of the dimples, while eV19t1, eV19t2, eV36t1, eV36t2, pV19t2 and pV36t2 break by a flat fracture mode. Furthermore, there are significant differences between the equiaxed and platelet morphologies. The equiaxed microstructures exhibit homogeneous dimple sizes. The platelet microstructures show some flat zones with fewer voids and with a parabolic shape. This indicates a local shearing mechanism [35] with less homogeneous void sizes. In the DENT cracked specimens, the micrographs are very similar to the fracture surfaces of tensile specimens and indicate a ductile mode of crack propagation as well. The mean void spacing was determined by image analysis. The segmentation of the void edges was performed by hand on SEM micrographs (2000x magnification) using translucent paper. The position of each void was then determined using an image analysis software (ImageJ). The results (see Supplementary Materials) show almost no significant variation among the different specimens, with a mean spacing between closest neighbors slightly larger than 1 $\mu$m, and with a slightly larger heterogeneity in sizes in the case of platelet microstructures, as given by the standard deviation.

The thickness reduction factor, $r_f$, and the equivalent fracture strain, $\varepsilon_{f,eq}$, for the DENT specimens are given in Table 8. The platelet-like DP steels demonstrate larger $r_f$ and $\varepsilon_{f,eq}$, except for the 36% $\alpha$' – 1mm thick sheet. The eV36t1 specimen corresponds to the particularly high EWF value.

Fig. 12 shows a comparison of the transverse sections extracted below the fracture surface of equiaxed and platelet-like DP steels. The platelet morphology exhibits a much lower density of voids. A similar observation was already made by Pierman [14] using 3D tomography (see Suppl. Mater.). The number of voids remains small even right below the fracture surface although the deformation is extremely large. The platelet-like DP steels are thus much more resistant to void nucleation and exhibits a much smaller void volume fraction (due to less and smaller voids, with a diameter around a few hundreds of nanometers). This is an important and partly unexpected finding of this study. The voids in the equiaxed DP steels are elongated in the direction of loading, indicating a long process of plastic void growth.

The void nucleation mechanisms involve decohesion of $\alpha$-$\alpha$' interface and fracture of $\alpha$' particles (see micrographs in Suppl. Mater.) with one mechanism dominating over the other depending on the microstructure. In the equiaxed microstructures, voids nucleate primarily by particle fracture, even though, on some occasions, voids develop along $\alpha$-$\alpha$' interfaces, as observed as well by Pierman [14]. In the platelet microstructures, voids nucleate primarily by decohesion along an interface perpendicular to the main loading direction located at the tip of the particle. In both cases, voids nucleate more often in zones of large $\alpha$' density, involving larger constraint in the $\alpha$ channels and at interfaces [36]. This is particularly evident between closely spaced $\alpha$' particles. Void nucleation by particle failure occurs late in the plastic regime.

An important final observation for the platelet morphology is shown in Fig. 13. Away from the fracture surface, the $\alpha$' platelets are randomly oriented (Fig. 13(b)). When moving close to the fracture surface, there is a progressive alignment/rotation along the loading direction. Just below the surface, the particles are almost perfectly aligned, see Fig. 13(c). Fig. 13(d) also indicates that in the event of a region fracturing under large shear, the particles rotate also towards the shear direction.

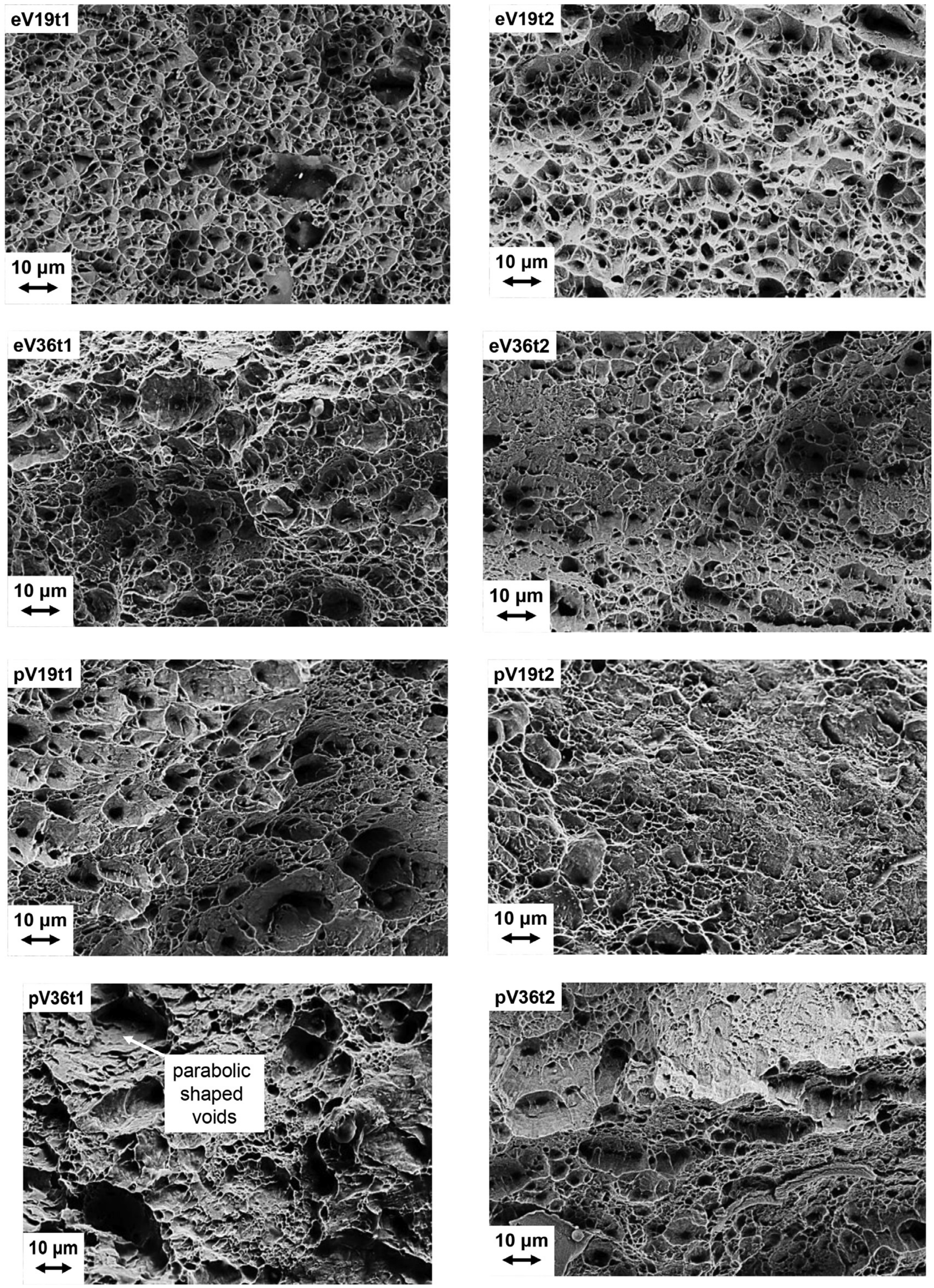


**Fig. 11.** SEM micrographs of the fracture surfaces of uniaxial tension specimens for the eight thin sheets microstructures.

## 4. Discussion

The platelet-like microstructure resists to cracking better than the corresponding equiaxed microstructure and the gain is amplified for increasing plate thickness. This is the core result of this study clearly evidenced in Fig. 9. This higher cracking resistance is translated into better hole expansion performances, thus proving the practical interest in a loading configuration representative of an important class of forming operations. It is worth noting that the hole expansion test quantifies the resistance to cracking initiation from preexisting edge defects induced by sheet cutting (and a small part of propagation as the test is continued until the crack propagates through the thickness of the sample), while the EWF is more related to the resistance to cracking during propagation. However, the failure mechanisms are essentially similar, differing only by minute variations of the stress state.

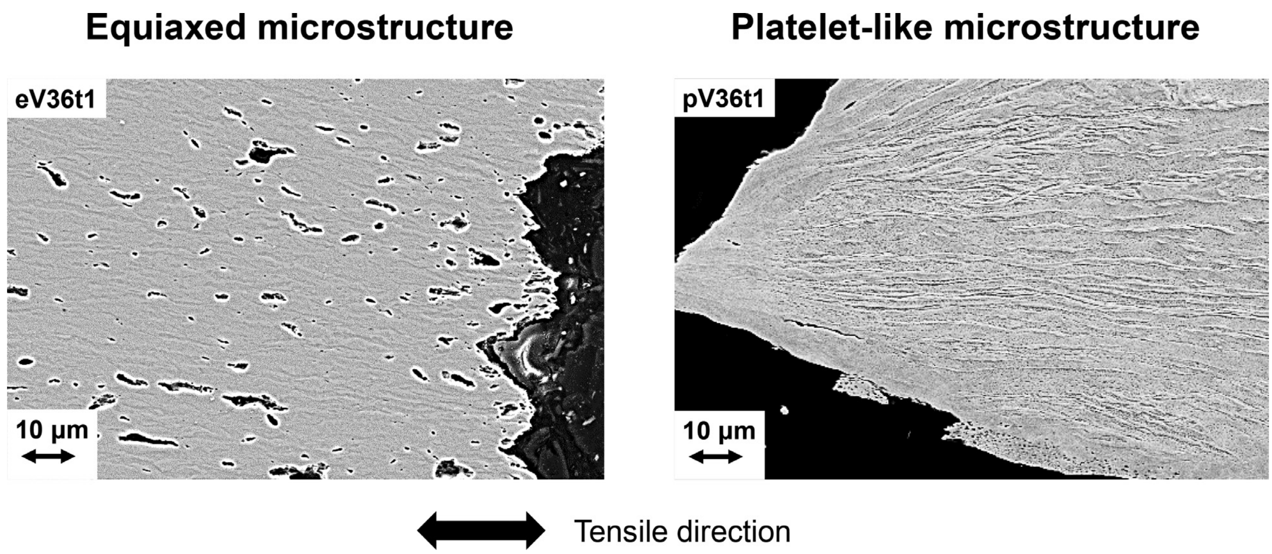


**Fig. 12.** SEM micrograph of a transverse section of a uniaxial tensile specimen of an equiaxed microstructure (eV36t1) and of a platelet-like microstructure (pV36t1).

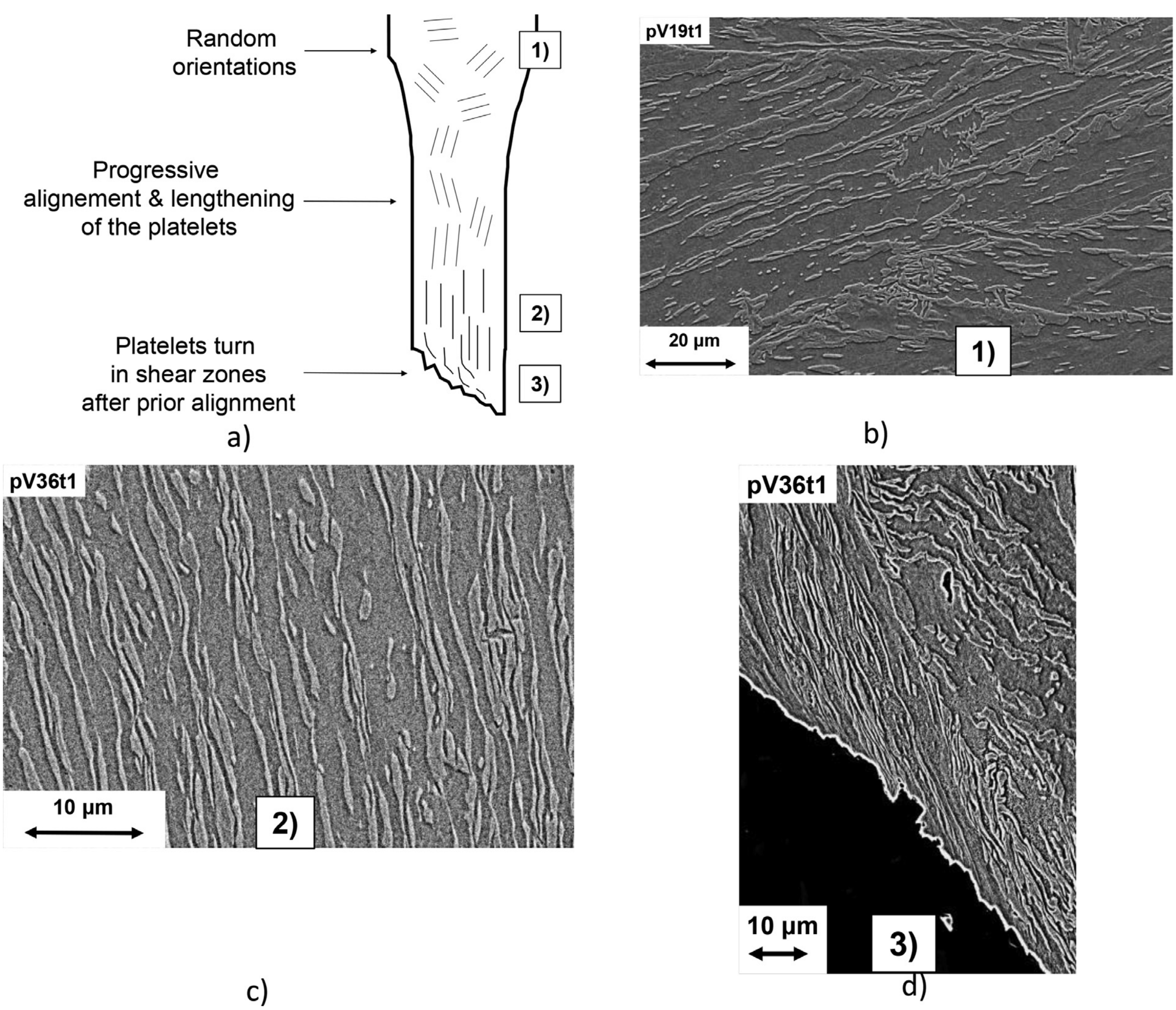


**Fig. 13.** (a) Schematic representation of a broken tensile specimen indicating where the SEM micrographs of (b), (c) and (d) are located.

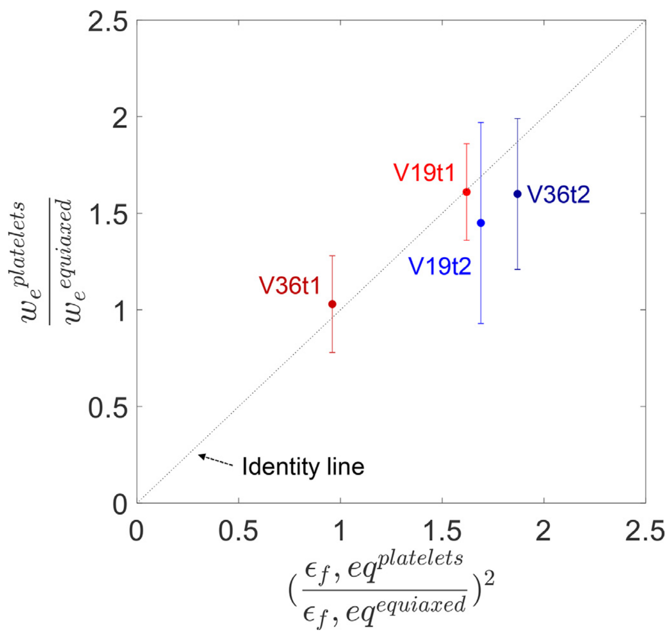


**Fig. 14.** Ratio of the essential work of fracture in a platelet-like microstructure and in an equiaxed microstructure as a function of the square of the corresponding ratio of the average equivalent fracture strain in DENT specimens, for a given martensite volume fraction and sheet thickness.

A large strength-ductility product, $\varepsilon_u\sigma_u$, of DP steels is often, but erroneously, taken as an indicator of a good fracture toughness. This conception is generally wrong as demonstrated here again, as well as in many recent works on different steels [1,21,37–39]. First, there is obviously no correlation to be expected between $w_e$ or $J_{Ic}$ and the product $\varepsilon_u\sigma_u$. The product $\varepsilon_u\sigma_u$ quantifies the energy associated to the resistance to plastic localization. The fact that this product is called "toughness" reinforces the confusion. The resistance to the onset of necking or to any sort of plastic localization is hardly related to the energy needed for damage growth and for material separation in the FPZ.

Now, as indirectly motivated by Eq. (1) or by relationships such as the Hahn-Rosenfield [40] empirical equation ($K_{Ic} \approx \sqrt{2\sigma_0 E^* n^2 \varepsilon_f}$), there is a direct correlation between the deformation capacity of the material measured by the true fracture strain $\varepsilon_f$, and the cracking resistance, quantified by $J_{Ic}$ or by the EWF, $w_e$. In rough terms, $w_e$ is proportional to the product $\varepsilon_f\sigma_f$. This relationship is not an equality because, as explained in the introduction, a microstructure length scale, $X_0$, also controls the amount of energy spent in the FPZ. Furthermore, $\sigma_f$ and $\varepsilon_f$ should be taken as the values corresponding to the stress state associated to the FPZ and not from a uniaxial tensile test (even in the case of thin sheets for which the stress triaxiality is lower than in plane strain cracked specimens, there is a significant difference of stress state [17]). At very large strains, the stress varies almost linearly with strain, so that $w_e$ should be almost proportional to $\varepsilon_f^2$ as $w_e \propto \varepsilon_f\sigma_f \propto \varepsilon_f^2$. Fig. 14 shows the variation of the $w_e$ of platelet-like DP steels normalized by the $w_e$ of the corresponding equiaxed steel (with the same $\alpha$' volume fraction and the same sheet thickness) as a function of the square of the corresponding $\varepsilon_{f,eq}$ of the platelet-like steel normalized by the square of the $\varepsilon_{f,eq}$ of the equiaxed steel. The fracture strain is the one measured on DENT specimens in order to be representative of the specific stress state in the cracked specimen. Fig. 14 supports the proposed relationship $w_e \propto \varepsilon_f\sigma_f \propto \varepsilon_f^2$, demonstrating that, as a first order trend, the enhanced cracking resistance of the platelet DP steels can be mainly explained by a larger $\varepsilon_f$.

This relationship brings several questions related to the specific behavior of the platelet morphology.

(1) Why is the platelet microstructure more resistant to damage accumulation, leading to large $\varepsilon_f$ (in particular at the higher stress triaxiality corresponding to the cracked specimens)?
(2) Why is the microstructure length scale, $X_0$, not playing a role, while, apparently, the characteristic dimensions of the microstructure look different?
(3) Why the specific specimen with 36% $\alpha$' and 1 mm thickness does not show such an improved $\varepsilon_f$, nor a significantly improved EWF in the case of the platelet morphology?

The resistance to damage accumulation in the case of the platelet morphology is primarily related to the delayed damage nucleation, as shown in Fig. 12. The first origin of this excellent void nucleation resistance is related to the mechanism of particle alignment. Indeed, this alignment of the $\alpha$' particles with the loading direction, schematized in Fig. 13(d), decreases the fraction of $\alpha$-$\alpha$' interface area perpendicular to the main loading direction. Since voids nucleate mainly by interface decohesion in the platelet-like microstructures, the resulting configuration leads to a reduction of the number of weak spots. Even though difficult to verify, the alignment can also possibly lead to an increase of the strain hardening at large strains, after the reorientation of the particles, hence increasing even more the dissipated energy. This speculation apparently contradicts the similar strain hardening capacities at large deformation shown in Fig. 7(a); but, as explained earlier, the linear evolution is only an approximation and the hardening rate could potentially be lower after necking and be boosted at larger strains. Independently of this possible impact on the strain hardening rate, the alignment is only made possible through the ability of the $\alpha$' particles to plastically deform up to large strains without breaking. Much earlier void nucleation by $\alpha$' fracture would of course not allow this mechanism to occur. The high ductility of the $\alpha$' platelets is most probably related to the small section of the particles, which increases the resistance to fracture. Indeed, particle size is known to largely affect void nucleation. Voids nucleate firstly on large second phase particles as the likelihood of containing internal defects (for particle fracture) or interfacial defects (for decohesion) increases gradually with particle size, e.g. [41–44]. A second reason for the larger fracture strain, directly related to the first one, is associated to the small void sizes in the platelet-like DP steels even at high strains. Strain gradient plasticity arguments tend to show that the growth rate of sub-micron-sized voids can be much slower than with large voids [45–48]. A final open question related to the alignment of the particles is about the impact of severe non-radial loadings, for instance a two-stage deformation path with large strain imposed during the first stage followed by a rotation of the main loading direction at 90°. The anticipated result would be a decrease of the fracture strain compared to a single stage radial or near radial loading. This point is worth exploring in future investigations.

The cracking resistance is, as explained with Eq. (1), related to the characteristic length, $X_0$. Although it is not equal to the initial void spacing, the mean spacing between closest dimples on a fracture surface constitutes a good indication to compare possible variations of this internal length scale. Note that it is more meaningful to look at closest neighbors instead of the mean spacing between neighbors as the void coalescence process is always dictated by closest voids. This analysis of the dimple spacing, while showing a much more heterogeneous distribution in the case of the platelet morphologies, did not highlight significant variations between platelet-like and equiaxed microstructures. This should also be related partly to the particle alignment effect, which tends to bring closer the nucleated voids in the case of the platelet-like steels. Hence, differences of $X_0$ cannot be invoked to justify the differences in cracking resistance, which could have been a plausible justification. It is worth noting that the more heterogeneous nature of the fracture surface of the platelet-like steels comes from the random initial orientation of the platelet packets.

Finally, explaining the specific behavior of the steel pV36t1 versus eV36t1 is not straightforward. The average $\varepsilon_{f,eq}$ is large for both the platelet-like (= 1.09) and equiaxed (= 1.11) steels. The EWFs of the two microstructures are close. A possible reason for the excellent behavior of the sample eV36t1 is its larger strength, which might be due to a higher degree of $\alpha$' interconnectivity, leading to a higher deformation accommodation by the hard $\alpha$'. Moreover, a higher $\alpha$' volume fraction can lead to a higher resistance to cracking, partly because the crack is then forced to propagate (and to deviate) through the interconnected hard phase [49]. Finally, increasing the $\alpha$' fraction for a given composition reduces the mechanical contrast between the phases, which could delay the appearance of damage. Indeed, decreasing the $\alpha$' hardness - by changing its composition, particularly its carbon content, or by tempering - leads to an increase of the fracture strain [13,50–53]. Lower stress incompatibilities at the interface lead to delayed nucleation and slower void growth rate [36,54–55]. This provides room for further improvement along different lines, beyond playing only with the $\alpha$' morphology.

In order to explore deeper the relationship between microstructure, plastic properties and cracking resistance of thin sheets, the different contributions influencing the EWF have to be scrutinized. Fig. 9 showed that the EWF, $w_e$, increases with thickness, $t_0$. In general, the cracking resistance first increases with $t_0$ at small $t_0$ because of a higher energy dissipated by necking, reaches a maximum and then decreases down to a steady value corresponding to the plane strain work of fracture (e.g. [17,56]). The microstructures investigated here lay in the range of $t_0$ in which $w_e$ increases linearly with $t_0$. The decomposition of $w_e$ into $\Gamma_0$ and $\Gamma_n$ cannot be quantitatively exploited due to the large uncertainty, but some qualitative aspects can be discussed. The term $\Gamma_n$ depends on $t_0$ and on $\beta w_n$, which takes into account the shape and size of the necking zone (through $\beta$) and the amount of work spent per unit volume $w_n$. The term $\beta w_n$, which quantifies the impact of thickness variation on the energy dissipated, is systematically larger for the platelet-like DP steels (see Table 6). The first reason is simply the larger fracture strain allowing more dissipation by necking near the crack tip (Table 8). The factor $\beta$ could also have an influence. This factor is directly related to the strain hardening capacity, since a larger strain hardening leads to a wider necking zone [17]. As mentioned above, it can be speculated that the $\alpha$' alignment at very large strains in the necking region may lead to higher strain hardening capacity and thus larger $\beta$ values, hence providing another source of toughening.

As a final point of discussion, it is worth comparing the cracking resistance versus fracture strain of the DP steels studied in this work to other steels and other metallic alloys in order to position their fracture performances. Fig. 15 shows a collection of $J_{Ic}$ and $w_e$ plotted as a function of $\varepsilon_f$ for various steels (DP steels, TRIP steels, CrMo steels, stainless steels) as well as for other metallic alloys (Al alloys, brass, zinc, bronze). The values are taken from the literature ([14,17,21,57,58]. Hardly any other alloys outperform or match the platelet-like DP steels investigated in the present study in terms of this set of properties, except stainless steels and multiphase TRIP steels, known for their high cracking resistance, but also for much more expensive chemical compositions. The general trend of cracking resistance increasing with fracture strain is obviously respected, knowing however that other factors play a role such as the strength and sheet thickness when dealing with thin sheets.

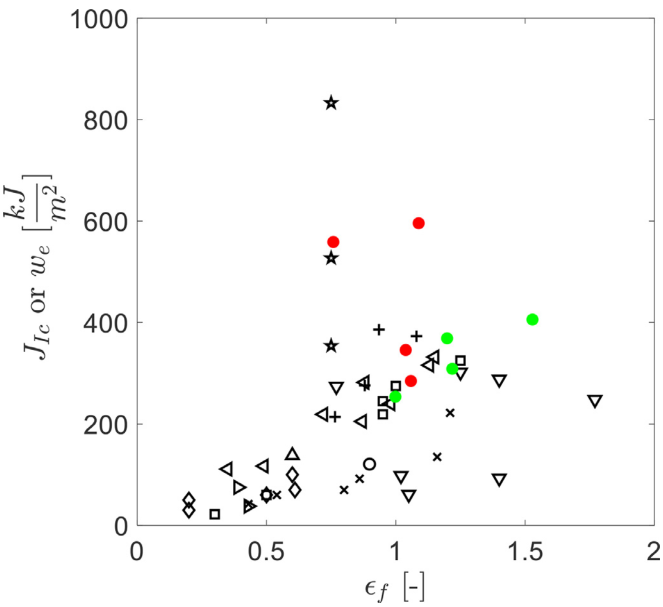


**Fig. 15.** Initiation fracture toughness, $J_{Ic}$, or essential work of fracture, $w_e$, as a function of fracture strain, $\varepsilon_f$, for various steels, but also other metals. Some platelet-like DP steels (red and green bold dots) compete with the toughest steels. Red dots represent the $w_e$ of platelet-like DP steels (present work), green dots represent the $J_{Ic}$ of platelet-like DP steels in thick sheets [14]. Diamonds are for the $J_{Ic}$ of platelet-like DP steels at high $V_{\alpha'}$ and/or high $C_{\alpha'}$ [14], crosses for the $J_{Ic}$ of TRIP steels in thin sheets [21], triangles pointing right for the $J_{Ic}$ of DP steels in thin sheets [21], squares for the $J_{Ic}$ of A533B, 12Cr-1Mo, 9Cr-2Mo, A508, 2.25Cr-1Mo steels and Cu-Be-Co alloy [57], triangles pointing left for the $J_{Ic}$ of 2.25Cr1Mo steel base material and weld, as received and after de-embrittlement, and of 1.25Cr0.5Mo, 40CrNi2Mo, 25CR2NiMo1V, 23CrNiMoWV steels [56], a circle for the $J_{Ic}$ of a short elongated DP steel [14], triangles pointing down for the $w_e$ of Al alloys, brass, bronze and zinc [17], stars for the $w_e$ of a A316L stainless steel [17], a '+' for the $w_e$ of equiaxed DP steels (present work), and a triangle pointing up for the $w_e$ of an equiaxed DP steel in a 1.4 mm thin sheet [11].

## 5. Conclusions

The cracking resistance of DP steels with 'Thomas fibers' platelet-like microstructure has been determined for different martensite volume fractions and sheet thicknesses, and compared to reference equiaxed microstructures, as well as contrasted with data on thick plane strain specimens. The analysis was based on the estimation of the EWF, critical CTOD, tensile tests and hole expansion tests, combined with systematic damage analysis of broken specimens. The main findings can be summarized as:

- The platelet microstructure shows a resistance to fracture typically 50% larger than the corresponding equiaxed reference. The resistance to cracking depends on the sheet thickness and martensite volume fraction. A significant part of the fracture energy results from crack tip necking in the case of thin sheets.
- The higher fracture toughness can be directly related to the larger fracture strain of the platelet morphology. Indeed, the fracture stress scales with fracture strain and no significant difference has been found regarding the characteristic void spacing for the different microstructures.
- The larger fracture strain of the platelet morphology originates primarily from the postponed nucleation of voids and the reduced void growth, leading to smaller void volume fractions. The resistance to void nucleation is favored by an excellent resistance of martensite platelets to fracture, most probably due to a small size, and to an alignment of the martensite particles along the main loading direction at large deformations.

• The better cracking resistance leads to improved stretch flangeability as measured by hole expansion tests, proving the interest of platelet-like DP steels for forming operations.

The present study shows that there is still room for improving the mechanical performances of DP steels by microstructure engineering, without playing with composition and thus without compromising the cost advantage. One perspective would be to optimize the characteristics of the platelets. A refined structure could potentially further delay the occurrence of damage while increasing the strength, even though it would occur at the expense of decreasing the characteristic length scale associated to the fracture process zone.

## Declaration of Competing Interest

The authors declare that they have no known competing financial interests or personal relationships that could have appeared to influence the work reported in this paper.

## Acknowledgments

This work was supported by ArcelorMittal and UCLouvain. Furthermore, the help of F. Hannard is gratefully acknowledged for the 3D reconstruction shown in Fig. 3.

## Supplementary materials

Supplementary material associated with this article can be found, in the online version, at doi:10.1016/j.actamat.2021.116700.

## References

[1] D. Casellas, A. Lara, D. Frómeta, D. Gutiérrez, S. Molas, L. Pérez, J. Rehrl, C. Suppan, Fracture toughness to understand stretch-flangeability and edge cracking resistance in AHSS, Metall. Mater. Trans. A 48 (2017) 86–94.
[2] J.I. Yoon, J. Jung, S.-H. Joo, T.J. Song, K.-G. Chin, M.H. Seo, S.-J. Kim, S. Lee, H.S. Kim, Correlation between fracture toughness and stretch-flangeability of advanced high strength steels, Mater. Lett. 180 (2016) 322–326.
[3] A. Bag, K.K. Ray, E.S. Dwarakadasa, Influence of martensite content and morphology on tensile and impact properties of high-martensite dual-phase steels, Metall. Mater. Trans. A 30 (1999) 1193–1202.
[4] A. Bag, K.K. Ray, E.S. Dwarakadasa, Influence of martensite content and morphology on the toughness and fatigue behavior of high-martensite dual-phase steels, Metall. Mater. Trans. A 32 (2001) 2207–2217.
[5] M. Calcagnotto, D. Ponge, D. Raabe, Effect of grain refinement to 1 $\mu$m on strength and toughness of dual-phase steels, Mat. Sci. Eng. A 527 (2010) 7832–7840.
[6] Y.J. Chao, J.D. Ward, R.G. Sands, Charpy impact energy, fracture toughness and ductile-brittle transition temperature of dual-phase 590 steel, Mater. Des. 28 (2007) 551–557.
[7] S.-M. Kang, H. Kwon, Fracture behavior of intercritically treated complex structure in medium-carbon 6Ni steel, Metall. Trans. A 18 (1987) 1587–1592.
[8] A. Bayram, A. Uguz, M. Ula, Effects of microstructure and notches on the mechanical properties of dual-phase steels, Mater. Charact. 43 (1999) 259–269.
[9] K.K. Alaneme, Fracture toughness (K1c) evaluation for dual phase medium carbon low alloy steels using circumferential notched tensile (CNT) specimens, electronic publication, Mater. Res. 14 (2011) 155–160.
[10] M. Faccoli, G. Cornacchia, M. Gelfi, A. Panvini, Notch ductility of steels for automotive components, Eng. Fract. Mech. 127 (2014) 181–193.
[11] D. Frómeta, S. Parareda, A. Lara, S. Molas, D. Casellas, P. Jonsén, J. Calo, Identification of fracture toughness parameters to understand the fracture resistance of advanced high strength sheet steels, Eng. Fract. Mech. 229 (2020) 106949.
[12] N.J. Kim, G. Thomas, Effects of morphology on the mechanical behavior of a dual phase Fe/2Si/0.1C steel, Metall. Trans. A 12 (1981) 483–489.
[13] A.P. Pierman, O. Bouaziz, T. Pardoen, P.J. Jacques, L. Brassart, The influence of microstructure and composition on the plastic behaviour of DP steels, Acta Mater. 73 (2014) 298–311.
[14] A.P. Pierman, Micromechanical study of the influence of the microstructure and composition on the plastic flow and damage properties of DP steels. Doctoral Thesis (2013).
[15] M. Sarwar, R. Priestner, Influence of ferrite-martensite microstructural morphology on tensile properties of dual-phase steel, J. Mater. Sci. 31 (1996) 2091–2095.
[16] T. Pardoen, J.W. Hutchinson, Micromechanics-based model for trends in toughness of ductile metals, Acta Mater 51 (2003) 133–148.
[17] T. Pardoen, F. Hachez, B. Marchioni, P.H. Blyht, Atkins, mode I fracture of sheet metal, J. Mech. Phys. Solids 52 (2004) 423–452.
[18] D. Frómeta, A. Lara, S. Molas, D. Casellas, J. Rehrl, C. Suppan, P. Larour, J. Calvo, On the correlation between fracture toughness and crash resistance of advanced high strength steels, Eng. Fract. Mech. 205 (2019) 319–332.
[19] S. Golling, D. Frómeta, D. Casellas, P. Jonsén, Investigation on the influence of loading-rate on fracture toughness of AHSS grade, Mat. Sci. Eng. A 726 (2018) 332–341.
[20] D. Gutiérrez, L. Pérez, A. Lara, D. Casellas, J.M. Prado, Toughness evaluation of high strength steels sheets by means of the essential work of fracture. ECF19 (2012).
[21] G. Lacroix, T. Pardoen, P.J. Jacques, The fracture toughness of TRIP-assisted multiphase steels, Acta Mater. 56 (2008) 3900–3913.
[22] S. Sahoo, N. Padmapriya, P.S. De, P.C. Chakraborti, S.K. Ray, Ductile tearing resistance indexing of automotive grade DP 590 steel sheets: EWF testing using DENT specimens, J. Mater. Eng. Perform. 27 (2018) 2018–2023.
[23] R. Sarkar, S.K. Chandra, P.S. De, P.C. Chakraborti, S.K. Ray, Evaluation of ductile tearing resistance of dual-phase DP 780 grade steel sheet from essential work of fracture (EWF) tests, Theor. Appl. Fract. Mech. 103 (2019) 102278.
[24] T. Pardoen, Y. Marchal, F. Delannay, Essential work of fracture compared to fracture mechanics – towards a thickness independent plane stress toughness, Eng. Fract. Mech. 69 (2002) 617–663.
[25] B. Cotterell, T. Pardoen, A.G. Atkins, Measuring toughness and the cohesive stress-displacement relationship by the essential work of fracture concept, Eng. Fract. Mech. 72 (2005) 827–848.
[26] B. Cotterell, J.K. Reddel, The essential work of plane stress ductile fracture, Int. J. Fract. 13 (1977) 267–277.
[27] G. Martin, S.K. Yerra, Y. Bréchet, M. Véron, J.-D. Mithieux, B. Chébab, L. Delannay, T. Pardoen, A macro- and micromechanics investigation of hot cracking in duplex steels, Acta Mater 60 (2012) 4646–4660.
[28] Y.W. Mai, K.M. Pilko, The essential work of plane stress ductile fracture of a strain-aged steel, J. Mater. Sci. 14 (1979) 386–394.
[29] Y.W. Mai, B. Cotterell, On the essential work of ductile fracture in polymers, Int J Fract. 32 (1986) 105–125.
[30] Y.W. Mai, P. Powell, Essential work of fracture and j-integral measurements for ductile polymers, J. Polym. Sci. B Polym. Phys. 29 (1991) 785–793.
[31] Y.W. Mai, On the plane-stress essential fracture work in plastic failure of ductile materials, Int. J. Mech. Sci. 35 (1993) 995–1005.
[32] T. Pardoen, F. Delannay, A method for the metallographic measurement of the CTOD at cracking initiation and the role of reverse plasticity on unloading, Eng. Fract. Mech. 65 (2000) 455–466.
[33] C.F. Shih, M.D. German, Requirements for a one parameter characterization of crack tip fields by the HRR singularity, Int. J. Fract. 17 (1981) 27–43.
[34] T.S. Byun, K. Farrell, M. Li, Deformation in metals after low-temperature irradiation: part I – mapping macroscopic deformation modes on true stress-dose plane, Acta Mater 56 (2008) 1044–1055.
[35] I. Barsoum, J. Faleskog, Rupture mechanisms in combined tension and shear – experiments, Int. J. Solids Struct. 44 (2007) 1768–1786.
[36] S.K. Yerra, G. Martin, M. Véron, Y. Bréchet, J.D. Mithieux, L. Delannay, T. Pardoen, Ductile fracture initiated by interface nucleation in two-phase elastoplastic systems, Eng. Fract. Mech. 102 (2013) 77–100.
[37] F. Hisker, R. Thiessen, T. Heller, Influence of microstructure on damage in advanced high strength steels, Mater. Sci. Forum 706-709 (2012) 925–930.
[38] Z. Xiong, P.J. Jacques, A. Perlade, T. Pardoen, Ductile and intergranular brittle fracture in a two-step quenching and partitioning steel, Scr. Mater. 157 (2018) 6–9.
[39] Z. Xiong, P.J. Jacques, A. Perlade, T. Pardoen, Characterization and control of the compromise between tensile properties and fracture toughness in a quenched and partitioned steel, Metall. Mater. Trans. A 50 (2019) 3502–3513.
[40] G.T. Hahn, A.R. Rosenfield, Sources of fracture toughness: the relation between KIc and the ordinary tensile properties of metals, In 'Applications related phenomena in titanium alloys', ed. H. Conrad, R. Jaffee, H. Kessler, and W. Minkler (West Conshohocken, PA: ASTM International) (1968) 5-32.
[41] M.D. Dighe, A.M. Gokhale, M.F. Horstemeyer, Effect of loading condition and stress state on damage evolution of silicon particles in Al-Si-Mg-base cast alloy, Metall. Mater. Trans. A 33 (2002) 555–565.
[42] J. Gurland, Observations on the fracture of cementite particles in a spheroidized 1.05% c steel deformed at room temperature, Acta Metall 20 (1972) 735–741.
[43] F. Hannard, T. Pardoen, E. Maire, C.L. Bourlot, R. Mokso, A. Simar, Characterization and micromechanical modelling of microstructural heterogeneity effects on ductile fracture of 6xxx aluminium alloys, Acta Mater 103 (2016) 558–572.
[44] J.J. Lewandowski, C. Liu, W.H. Hunt, Effects of matrix microstructure and particle distribution on fracture of an aluminum metal matrix composite, Mat. Sci. Eng. A 107 (1989) 241–255.
[45] U. Borg, C.F. Niordson, J.W. Kysar, Size effects on void growth in single crystals with distributed voids, Int. J. Plast. 24 (2008) 688–701.
[46] B. Liu, X. Qiu, Y. Huang, K.C. Hwang, M. Li, C. Liu, The size effect on void growth in ductile materials, Int. J. Plast. 51 (2003) 1171–1187.
[47] B. Liu, Y. Huang, M. Li, K.C. Hwang, C. Liu, A study of the void size effect based on the Taylor dislocation model, Int. J. Plast. 21 (2005) 2107–2122.
[48] V. Tvergaard, C. Niordson, Nonlocal plasticity effects on interaction of different size voids, Int. J. Plast. 20 (2004) 107–120.
[49] J. Samei, Y. Salib, M. Amirmaleki, D.S Wilkinson, The role of microstructure on edge cracks in dual phase and quench and partitioning steels subject to severe cold rolling, Scr. Mater. 173 (2019) 86–90.

[50] M. Azuma, S. Goutianos, N. Hansen, G. Winther, X. Huang, Effect of hardness of martensite and ferrite on void formation in dual phase steel, Mater. Sci. Technol. 28 (2012) 1092–1100.
[51] M. Mazinani, W.J. Poole, Effect of martensite plasticity on the deformation behavior of a low-carbon DP steel, Metall. Mater. Trans. A 38 (2007) 328–339.
[52] G.R. Speich, R.L. Miller, Mechanical properties of ferrite-martensite steels, Struct. Properties Dual Phase Steels (1979) 145–182.
[53] Y. Tomota, H. Yoshino, K. Kuroki, Effect of ductility of second phase on ductile fracture, Scr. Metall. 11 (1977) 853–856.
[54] T.W.J. de Geus, F. Maresca, R.H.J. Peerlings, M.G.D. Geers, Microscopic plasticity and damage in two-phase steels: on the competing role of crystallography and phase contrast, Mech. Mater. 101 (2016) 147–159.
[55] C. Landron, O. Bouaziz, E. Maire, J. Adrien, Characterization and modeling of void nucleation by interface decohesion in dual phase steels, Scr. Mater. 63 (2010) 973–976.
[56] T. Pardoen, Y. Marchal, F. Delannay, Thickness dependence of cracking resistance in thin aluminium plates, J. Mech. Phys. Solids (1999) 2093–2123.
[57] K. Guan, L. Hua, Q. Wang, X. Zou, M. Song, Assessment of toughness in long term service CrMo low alloy steel by fracture toughness and small punch test, Nucl. Eng. Des. 241 (2011) 1407–1413.
[58] X. Mao, H. Takahashi, T. Kodaira, Supersmall punch test to estimate fracture toughness $J_{Ic}$ and its application to radiation embrittlement of 2.25Cr-1Mo steel, Mat. Sci. Eng. A 150 (1992) 231–236.